THE ASTROPHYSICAL JOURNAL, 422:336–350, 1994 February 10

PROPERTIES OF A B0 I STELLAR WIND AND INTERSTELLAR GRAINS DERIVED FROM *GINGA* OBSERVATIONS OF THE BINARY X-RAY PULSAR 4U 1538−52

GEORGE W. CLARK AND JONATHAN W. WOO
Center for Space Research and Department of Physics, Massachusetts Institute of Technology, Cambridge, MA 02139
AND
FUMIAKI NAGASE
Institute of Space and Astronautical Science, 3-1-1, Yoshinodai, Sagamihara, Kanagawa 229, Japan
Received 1992 July 13; accepted 1993 August 20

ABSTRACT

From measurements of the X-ray eclipse phenomena of the binary X-ray pulsar 4U 1538−52, we derive properties of the stellar wind of its B0 I companion, QV Nor, and a constraint on models of interstellar grains. Estimates of the wind density as a function of the distance from the center of QV Nor are obtained from an analysis of the variation of X-ray attenuation during an eclipse egress. The analysis takes account of the effects of X-ray ionization on the photoelectric absorption cross sections and yields a particle-number density described by the function $\Psi\{1 + (r/r_1)^2 \exp [-(r - r_1)/h]\}/(4\pi r^2 \mu)$ with $\Psi = 6.7 \times 10^{-10}\ M_\odot\ \mathrm{yr}^{-1}\ \mathrm{km}^{-1}\ \mathrm{s}$, $h = 4.3 \times 10^{10}$ cm, and $r_1 = 1.2 \times 10^{12}$ cm, where $\mu = 1.34 m_H$ is the average atomic mass per hydrogen atom. A Monte Carlo computation of the absorption and scattering of X-rays in the X-ray–ionized wind accounts for approximately two-thirds of the spectrum of X-rays with energies above 4.5 keV observed during the eclipse. Addition of density enhancements, like those predicted by a numerical computation of the hydrodynamic disturbance caused by passage of the neutron star through the wind, brings the predicted eclipse spectrum into agreement with the observed spectrum above 4.5 keV. Below 4.5 keV there is a component of soft X-rays above the Monte Carlo prediction with a total photon flux amounting to approximately 1.4% of the average uneclipsed flux in the same energy range. The intensity of the soft component exhibits an initial downward trend following eclipse ingress as expected of a component scattered by interstellar dust grains. Thermal emission from uneclipsed, shock-heated circumstellar matter is probably also present in the soft component. Taking the entire soft component as an upper limit on the intensity of the grain-scattered X-rays, and comparing this limit with the optical extinction of QV Nor, we derive an upper limit on a quantity $R_{XV}(E)$ which we call the scattering/extinction ratio of interstellar dust grains and define as $(E/1\ \mathrm{keV})^2$ times the ratio of the optical depth for scattering X-rays of energy E to the total optical extinction. In the Rayleigh-Gans approximation to the X-ray scattering efficiency, this quantity is independent of energy. Our upper limit on R_{XV} is 0.06 mag^{-1}, which implies that the X-ray scattering efficiency of interstellar dust is less than expected for solid grains with a size distribution of the form $n_g(a) \sim a^{-3.5}$ in the range from 0.005 to 0.25 μm and composed of silicate ($R_{XV} = 0.22\ \mathrm{mag}^{-1}$) or a silicate-graphite mixture ($R_{XV} = 0.11\ \mathrm{mag}^{-1}$) as derived from the calculations of Martin & Rouleau (1991). This lends support to the idea (Mathis & Whiffen 1989) that interstellar grains are "fluffy" aggregates with an average bulk density less than that of their constitutent particles. Such aggregates would have a smaller ratio of X-ray scattering efficiency to optical extinction efficiency compared with solid grains of the same material.

Subject headings: binaries: eclipsing — dust, extinction — pulsars: individual (4U 1538−52) — stars: mass loss — X-rays: stars

1. INTRODUCTION

The eclipse phenomena of massive X-ray binaries are sources of unique information about the atmospheric structures of their primaries. The latter are generally massive O or B0 stars with intense radiatively driven supersonic winds. Measurements of X-ray eclipse transitions probe the density structures of these winds over the range of radius in which the flow accelerates from near-rest to low supersonic velocities. In several of the massive X-ray binaries whose eclipse transitions have been analyzed for this purpose, the average runs of density in this range are found to conform to exponential functions of radius with scale heights of the order of a tenth of the stellar radii, in disagreement with the density functions derived in steady state theories of radiatively driven winds based on the Sobolev approximation. X-ray eclipse transition measurements therefore provide clues for the development of more realistic theories that avoid the Sobolev approximation and take account of instabilities in the radiation-driving mechanism.

The X-rays observed in eclipse cast light on several aspects of the circumsource and interstellar environment. Circumsource material scatters X-rays into the umbra with a spectrum similar in shape to that of the average uneclipsed spectrum and an intensity that is a measure of the ratio of the mass-loss rate to the terminal velocity of the wind. X-ray–excited fluorescence and thermal emission from the same matter, excited by the pulsar X-rays and by shock heating, contribute a soft continuum and emission lines. Scattering from interstellar grains produces a halo around the pointlike source that persists during an eclipse due to transit time delays. And, finally, the primary

star itself is a source of coronal X-rays, though generally of such relatively low intensity as to be negligible in comparison with the direct or secondary effects of the pulsar radiation.

Our purpose in this investigation was to derive from the X-ray eclipse phenomena of 4U 1538−52 properties of the stellar wind of its heavily reddened B0 I companion, QV Nor. We sought a model of the pulsar X-ray emission spectrum and the distribution of X-ray–ionized circumsource matter that yields a comprehensive explanation of the X-ray phenomena of the system. In addition, we derived a constraint on the density of interstellar grains from an analysis of the X-ray spectrum in eclipse and the optical extinction of QV Nor.

Lucy & Solomon (1970) suggested that radiation pressure due to scattering of stellar ultraviolet radiation in Doppler-shifted resonance absorption lines drives the cool ($T \sim 10^{4.6}$ K) winds of early-type stars to supersonic velocities with mass-loss rates of the order of $10^{-6}\ M_\odot\ \mathrm{yr}^{-1}$. Steady state theories based on this idea stem in large part from the work of Castor, Abbott, & Klein (1975), who developed a model that takes account of the multiplicity of UV resonance lines and conforms to the condition of a smooth transition from subsonic to supersonic flow. Their theory and later refinements (e.g., Abbott 1980, 1982; Friend & Abbott 1986) employed the Sobolev approximation, in which it is assumed that the density and other parameters that characterize the flow are approximately constant over distances in which the flow velocity increases by an ion thermal speed (Cassinelli 1979 and references therein). Steady state theories predict velocity functions in the supersonic regimes of early-star winds and mass-loss rates that are in general agreement with observations of ultraviolet P Cygni line profiles. Velocity curves derived in these theories have often been represented by a power law of the form

$$v = v_t(1 - r_0/r)^\beta\ , \quad r > r_0\ , \tag{1.1}$$

where r_0 is the radius of the stellar "surface", v_t is the terminal velocity, and β is in the range 0.5–1.5. With $\beta = 0.5$ this function represents the velocity of an isolated particle starting from rest at r_0 and driven outward by a force diminishing as the square of the distance. It implies a rapid initial acceleration and a corresponding rapid initial decline in the density. However, in the case of P Cygni itself, Van Blerkom (1978) concluded from an analysis of the profiles of the Balmer lines that "a substantial region of gradual acceleration is required; in fact, the entire line-forming portion of the envelope may lie in this region."

The Sobolev approximation is grossly inaccurate in the subsonic regime. Moreover, the steady state assumption is belied by the ubiquitous coronal X-ray emission of early-type stars (Cassinelli et al. 1981), which has been attributed to localized heating by shocks that arise from instabilities inherent in the radiation-driving mechanism (Lucy & White 1980). Nonsteady flow in the supersonic region is also revealed directly by the observation of variable discrete narrow absorption features within P Cygni profiles (Prinja, Howarth, & Henrichs 1987). This evidence of nonsteady flow implies that the density function which one can infer from a column density profile measured during an X-ray eclipse transition is a path average over a spectrum of density fluctuations.

To demonstrate the relevance of eclipsing X-ray binaries to the investigation of the structure of stellar winds, we estimate the wind velocity in the region probed by the analysis of X-ray attentuation during an eclipse transition. The column density of hydrogen atoms along a line of sight that passes the primary at a distance r where the particle density is $n(r)$ can be estimated as $N_\mathrm{H} \approx nr$. If the wind velocity at this radius is v, then the mass-loss rate is $\dot{M} = 4\pi r^2 \mu n v$, where $\mu = 1.34 m_\mathrm{H}$ is the average atomic mass per hydrogen atom. Solving for the velocity, we find

$$v \approx 23\left(\frac{\dot{M}}{10^{-6}\ M_\odot\ \mathrm{yr}^{-1}}\right)\left(\frac{N_\mathrm{H}}{10^{24}\ \mathrm{cm}^{-2}}\right)^{-1}\left(\frac{r}{10^{12}\ \mathrm{cm}}\right)^{-1} \mathrm{km\ s}^{-1}\ . \tag{1.2}$$

The column density for $1/e$ attenuation of an X-ray beam in cold matter with normal cosmic abundances ranges from $\sim 10^{23}$ to $\sim 10^{24}$ H atoms cm^{-2} in the energy range from 3.9 to 15.6 keV. The isothermal velocity of sound at 4×10^4 K is ~ 20 km s^{-1}. Thus, measurements of the changes in the X-ray spectrum in this energy range during an eclipse transition probe the density profile of the wind in the region of transition from subsonic to supersonic flow where the singularity in the hydrodynamic equation for steady flow occurs.

The fractional intensity of X-rays in eclipse due to Compton scattering by matter in a wind that moves with nearly its terminal velocity in the region beyond the orbit of the pulsar can be estimated as

$$\frac{\sigma_\mathrm{T}\dot{M}}{2\pi\mu v_t s} \approx 0.015\left(\frac{\dot{M}}{10^{-6}\ M_\odot\ \mathrm{yr}^{-1}}\right)\left(\frac{v_t}{2 \times 10^3\ \mathrm{km\ s}^{-1}}\right)^{-1} \times \left(\frac{s}{10^{12}\ \mathrm{cm}}\right)^{-1}\ , \tag{1.3}$$

where σ_T is the Thomson cross section and s is the distance between the star centers. Thus, with a stellar wind typical of B0 supergiants like the companion of 4U 1538−52, one can expect the Compton-scattered component of the X-ray intensity in eclipse to have a spectrum similar to the average uneclipsed spectrum with an intensity proportional to $\dot{M}/v_t$ and $\sim 1\%$–2% of the uneclipsed intensity.

The first observations of a column density profile during an X-ray eclipse transition in a massive X-ray binary were reported from *Uhuru* observations of Cen X-3 by Schreier et al. (1972), who found an exponential scale height of $h \approx 5 \times 10^{10}$ cm for the atmosphere of its companion. In addition, they found a residual intensity in the eclipse on the order of 1% of the uneclipsed intensity. More extensive studies of the eclipse transitions of Cen X-3 and their implications for the structure of the stellar wind of the primary were made with *SAS 3* (Clark, Minato, & Mi 1988) and *EXOSAT* (Day & Stevens 1993), with similar results concerning the exponential form of the lower atmospheric density and the magnitude of its scale height. X-ray eclipse transitions have been studied in Vela X-1 by Sato et al. (1986) and Lewis et al. (1992), and in 4U 1538−52 by Makishima et al. (1987), with results that are fitted by exponential density functions in the lower atmospheres of the companion stars with scale heights of the order of a tenth of the stellar radii. On the other hand, Haberl, White, & Kallman (1989) found that the column density profile of the wind in the O6.5f companion of 4U 1700−37 can be fitted throughout by a curve derived from a velocity function of the form of equation (1.1).

Finally, we emphasize a point made by Xu, McCray, & Kelley (1986) that an eclipsing X-ray binary offers a unique advantage for the study of interstellar grains. Since the optical extinction and the intensity of grain-scattered X-rays depend

on the size, composition, and density of the grains in quite different ways, a determination of the quantitiative relation between these two observables can place a critical constraint on models of interstellar grains. The angular distribution of X-rays in the image of an X-ray source consists of a "core" component that comes directly from the star or its immediate vicinity, and a generally much fainter "halo" component that has been scattered by interstellar grains near the line of sight, as predicted by Overbeck (1965) and discussed by him and others (Hayakawa 1970; Martin 1970) before the availability in orbit of imaging X-ray telescopes. Measures of the intensities of Overbeck halos have since been derived from analyses of X-ray star images in which the halo is dissected from the much brighter core by subtracting the point-spread function of the telescope (e.g., Catura 1983; Mauche & Gorenstein 1986, hereafter MG; Predehl et al. 1991). In addition, the halo intensity of a source near the Galactic center has been measured with a nonimaging detector during a brief time following a lunar occultation of the core component (Mitsuda et al. 1990). In the case of an eclipsing binary at a distance of several kiloparsecs the halo will persist long after the neutron star is eclipsed by its primary because the average travel time of the grain-scattered X-rays is many hours longer than the travel time of the undeviated X-rays in the core. Since the X-ray scattering efficiency of small particles varies as E^{-2}, the spectrum of the grain-scattered X-rays is much softer than the uneclipsed core spectrum. Consequently, when the core intensity is reduced by the eclipse, the grain-scattered X-rays may stand out in the spectrum as a "soft component" that decays with time after ingress. Analysis of high-resolution X-ray images of binary X-ray stars in eclipse will clearly be the best way to exploit such opportunities in the future. Nevertheless, we have derived significant results from an analysis of nonimaging data obtained during the X-ray eclipse of 4U 1538−52/QV Nor, a system which is especially favorable for such a study because of its high optical extinction.

In § 2 we describe the observations and data reduction. Section 3 presents our interpretation of the results in terms of the circumsource and interstellar environment, and the implications concerning stellar winds and the properties of interstellar grains. Section 4 is a summary.

2. OBSERVATIONS AND DATA ANALYSIS

We observed 4U 1538−52 from 1988 February 29 to March 3 with the large-area gas proportional counter (LAC) of the *Ginga* satellite X-ray observatory. The observatory has been described by Makino et al. (1987), and details of the LAC detector have been given by Turner et al. (1989). The LAC had a 1°.1 × 2°.0 FWHM field of view and an effective area of 4000 cm^2. Pulse-height distributions (PHDs) were recorded with various time resolutions from 0.5 to 16 s in 48 channels and with channel widths equivalent to 0.58 keV from 0 to 18.6 keV and channel widths equivalent to 1.16 keV from 18.6 to 37.2 keV. The energy resolution of the LAC detector was 20% FWHM at 5.9 keV. The energy–to–pulse-height transfer function is represented by a response matrix of 48 × 700 elements that specify the probability that a photon of energy E_j (j = 1–700) traversing the effective area of the LAC detector will produce a pulse registered in ith pulse-height channel (i = 1–48).

Discovery in these data of a cyclotron absorption line centered at 20 keV has been reported previously (Clark et al. 1990). Here we describe our analysis of the eclipse phenomena. To avoid complications in the spectrum arising from the cyclotron resonance, we confine the present analysis to the data in channels 27 and below (corresponding to energies ≤15.6 keV), which carry most of the information regarding the attenuation and scattering of the X-rays by the atmosphere of the primary. Values of the system parameters of 4U 1538−52 assumed in our analysis are summarized in Table 1.

Three adjustments were made to each transmitted PHD. Particle-induced background was subtracted according to the algorithm developed by Hayashida et al. (1989) from an analysis of the orbital dependence of the background rate. Next we subtracted the contribution of the diffuse cosmic X-ray background from the galactic ridge which was assessed as the PHD (corrected for particle background) observed when the field of view was shifted 2° at constant b toward higher l. This comparison field contains no source in the *HEAO 1* sky survey (Wood et al. 1984), the sensitivity limit of which (~0.001 counts cm^{-2} s^{-1}) is approximately 2% of the average uneclipsed count rate of 4U 1538−52 in the same energy range. Finally, to reduce the contribution from X-rays that did not come directly from the neutron star, we subtracted the average deep-eclipse PHD from the background-corrected PHDs.

In view of the uncertainty as to whether there are fainter undetected sources in the diffuse background comparison field, we cannot be sure that our eclipse PHDs, whose intensities are of the order of 2% of the uneclipsed intensities, have been accurately corrected for diffuse background. Nevertheless, the similarity in shape of the uneclipsed and eclipsed PHDs above 4.5 keV, and significant variations in the count rates observed over the duration of the eclipse, are evidence that some or most of the background-subtracted eclipse PHDs are produced by X-rays from the 4U 1538−52/QV Nor system.

2.1. *Variation of the Intrinsic Source Spectrum with Pulse Phase*

Derivation of information about column density along the line of sight to the neutron star is complicated by the variation of the intrinsic source spectrum with pulse phase. To circumvent this complication, we derived for each data-accumulation interval a nominal average source spectrum according to the following scheme. We first compiled the average pulse-phase–resolved PHD for each of 16 equal intervals of pulse phase from data recorded out of eclipse between orbital phases 0.28 and 0.45 when the attenuation appears to be steady and near

TABLE 1

PARAMETERS OF THE BINARY SYSTEM 4U 1538−52/QV NORMAE
(l = 327°.4; b = 2°.1)

Parameter	Value	Note
P_{orb}	3.72844 ± 0.00002 days	
$a_X \sin i$	(1.53 ± 0.11) × 10^{12} cm	1
Inclination	~70°	2
M_{opt}/M_X	16.1 ± 1.2	3
θ_e (eclipse half-angle)	28°.3 ± 0°.5	4
r_0 (primary radius)	(0.97 ± 0.12) × 10^{12} cm	5
P_{pulse}	530.43 ± 0.014 s	1
L_X (1–15 keV)	(2.9 ± 0.2) × 10^{36} ergs s^{-1}	4
L_{opt}	(6.2 ± 2.0) × 10^{38} ergs s^{-1}	3
Spectral type	B0 I	6
A_V	6.5 mag	6
Distance	5.5 ± 1.5 kpc	6

NOTES.—(1) Corbet, Woo, & Nagase 1993. (2) Assuming that the primary fills 90% of its Roche lobe. (3) Reynolds, Bell, & Hilditch 1992. (4) This work. (5) Derived. (6) Crampton, Hutchings, & Cowley 1978.

its minimum value. To each pulse-phase–resolved PHD in channels 8–27 (3.9–15.6 keV) we fitted a computed PHD derived as a convolution of the LAC response matrix and a spectrum of the form of the "broken power law"

$$
\begin{aligned}
I(E) &= I_0 \exp\left[-\sigma(E)N_{\rm H}\right]E^{-\alpha_1}, && E < E_1, \\
I(E) &= I_0 \exp\left[-\sigma(E)N_{\rm H}\right]E_1^{-\alpha_1}\left(\frac{E}{E_1}\right)^{-\alpha_2}, && E_1 < E < E_c \\
I(E) &= I_0 \exp\left[-\sigma(E)N_{\rm H}\right]E_1^{-\alpha_1}\left(\frac{E}{E_1}\right)^{-\alpha_2} && \\
&\quad \times \exp\left[-\frac{(E-E_C)}{E_f}\right], && E_c < E,
\end{aligned}
\tag{2.1}
$$

plus a Gaussian emission line representing the iron line centered at $E_{\rm Fe}$ with a width $\sigma_{\rm Fe}$. For the attenuation cross section $\sigma(E)$ we used the sum of the Thomson scattering cross section and the photoelectric absorption cross section of cold matter with normal cosmic abundances given by Morrison & McCammon (1983). In a preliminary analysis we found that the fitted values of the nominal column density, $N_{\rm H}$, clustered around 2.0×10^{22} H atoms cm^{-2} of cold matter, of which $\sim 1.6 \times 10^{22}$ H atoms cm^{-2} is attributable to the interstellar attenuation estimated from the optical extinction of QV Nor, $A_V \approx 6.5$ mag (Crampton, Hutchings, & Cowley 1978) and the relationship between extinction and column density (Gorenstein 1975). We interpret the remaining 0.4×10^{22} H atoms cm^{-2} as the average nominal column density of the portion of the QV Nor atmosphere along the line of sight to the neutron star during the low-absorption interval of orbital phase. In addition, we found the fitted value of the energy of the iron emission line clustered around 6.4 keV, and the width was not resolved. For the sake of uniformity we therefore fixed the values of $N_{\rm H}$, $E_{\rm Fe}$, and $\sigma_{\rm Fe}$ at 2.0×10^{22} H atoms cm^{-2}, 6.4 keV, and zero, respectively. Listed in Table 2 are the values of seven adjustable parameters and reduced χ^2 values of the fits for each of the 16 pulse-phase–resolved intervals. The line labeled UE$_{\rm av}$ lists the fitted parameters for the average PHD derived from the low-attenuation data. (The generally low reduced χ^2 values indicate that the nominal channel-width uncertainty of 1% for the LAC detector is overestimated.)

The low-absorption PHD averaged over the pulse phase is displayed in Figure 1 together with the fitted distribution in channels 8–27 derived as in the previous fittings from the spectrum of equation (2.1). The extension of the fitted PHD below channel 8, based on the same energy-spectrum parameters and $N_{\rm H} = 2.0 \times 10^{22}$ H atoms cm^{-2} of cold matter, is indicated by the dashed portion of the histogram. The X-ray energy flux in the range 1–15 keV implied by the parameters listed in Table 2 (with $N_{\rm H} = 0$) is $(8.1 \pm 0.5) \times 10^{-10}$ ergs cm^{-2} s^{-1}, and the corresponding luminosity for an assumed distance of 5.5 kpc is $(2.9 \pm 0.2) \times 10^{36}$ ergs s^{-1}, with error estimates in both values derived from the errors of the spectrum parameters listed in Table 2.

The difference between the dashed histogram and the observed count rates in channels 3–7, corresponding to calibration energies in the range 1.1–3.9 keV, is the soft excess mentioned previously. The solid-line histogram extending below channel 8 in Figure 1 shows the fit obtained by adding to the previously fitted spectrum a term of the form $I_1(E_0/E)$ exp $[-E/kT - \sigma(E)N_{\rm H}]$, with $I_1 = 1.1 \times 10^4$ s^{-1} keV^{-1}, $E_0 = 1$ keV, $kT = 0.37$ keV, and $N_{\rm H} = 2.0 \times 10^{22}$ H atoms cm^{-2}. The energy flux on the soft excess in the range 1.5–10 keV ($N_{\rm H} = 0$) is 2.8×10^{-11} ergs cm^{-2} s^{-1}, and the corresponding source luminosity is 1.0×10^{35} ergs s^{-1}.

In the next step of our analysis we partitioned all the data into PHDs accumulated from continuous observation intervals of approximately 1 pulse period ($\sim$530 s), or less if the observation was interrupted by Earth occultation, interference by trapped radiation, or other causes. For each accumulation interval we synthesized a low-attenuation PHD as a weighted average of the phase-resolved PHDs, with weight proportional to the exposure time in each of the 16 pulse-phase intervals. To this synthesized PHD in channels 8–27 we fitted a computed PHD derived as a convolution of the LAC response matrix and equation (2.1) with $N_{\rm H}$ fixed at 2.0×10^{22} H atoms cm^{-2}. The resulting spectrum parameters (with $N_{\rm H} = 0$) represent the unnormalized average source spectrum for the interval. Finally, we fitted to the accumulated PHD in channels 8–27 a

TABLE 2

PARAMETERS OF "BROKEN POWER LAWS" CHARACTERIZING THE 16 PHASE-RESOLVED INCIDENT SPECTRA[a]

Phase Bin Number	I_0 (photons s^{-1} keV^{-1})	α_1	E_1 (keV)	α_2	E_c (keV)	E_f (keV)	$I_{\rm Fe}$ (photons s^{-1})	χ^2_ν
1	106.4	1.01	6.0	0.44	5.2	7.5	2.2	1.12
2	127.7	1.23	9.9	0.52	11.8	10.2	1.8	0.96
3	103.4	0.96	9.4	0.36	12.6	10.0	1.1	1.20
4	104.8	0.96	9.1	0.38	12.5	9.0	1.4	1.00
5	174.7	1.20	7.7	0.84	13.0	7.3	2.3	0.66
6	44.4	0.27	4.6	1.10	12.2	7.2	1.8	1.00
7	123.8	1.26	8.8	1.00	11.8	9.2	1.4	0.53
8	244.3	1.69	10.8	1.10	13.0	6.5	1.6	1.45
9	236.6	1.51	7.3	1.69	13.0	14.9	1.1	1.70
10	415.3	1.56	10.5	0.63	12.1	8.1	0.7	0.58
11	269.2	1.19	9.5	0.46	11.6	9.5	0.0	0.52
12	221.4	1.03	8.4	0.79	12.3	14.6	0.8	0.67
13	281.9	1.18	6.3	0.74	12.6	20.6	3.1	0.36
14	234.9	1.08	8.8	0.60	13.0	19.7	0.6	0.84
15	403.8	1.42	10.2	0.69	13.3	13.9	0.8	0.64
16	231.8	1.17	5.0	1.52	9.4	16.3	0.8	0.42
UE$_{\rm av}$	194.9 $\pm$ 5.7	1.19 $\pm$ 0.02	9.4 $\pm$ 0.6	0.85 $\pm$ 0.12	12.5 $\pm$ 0.4	12.8 $\pm$ 1.6	1.2 $\pm$ 0.3	0.24

[a] The column density, $N_{\rm H}$, was fixed at the value 2.0×10^{22} H atoms cm^{-2} that was fitted to the phase-averaged data (UE$_{\rm av}$). The bottom line shows errors for the phase-averaged spectrum which are also typical of the phase-resolved spectra.

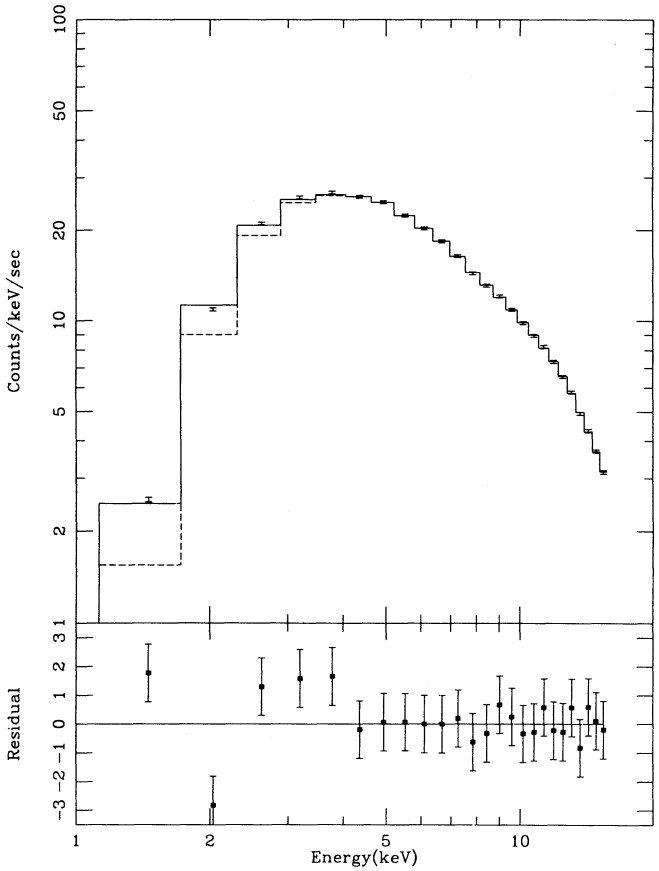

FIG. 1.—Average PHD of X-rays recorded during the orbital phase interval from 0.28 to 0.45 when the attenuation was near its minimum value. The fitted PHD (*solid line*) is derived from a spectrum of the form of eq. (2.1) of the text with the parameter values listed in Table 2 in the row labeled UE_{av}. Extension of the fitted PHD to channels below 7 exposes a soft excess in the uneclipsed spectrum.

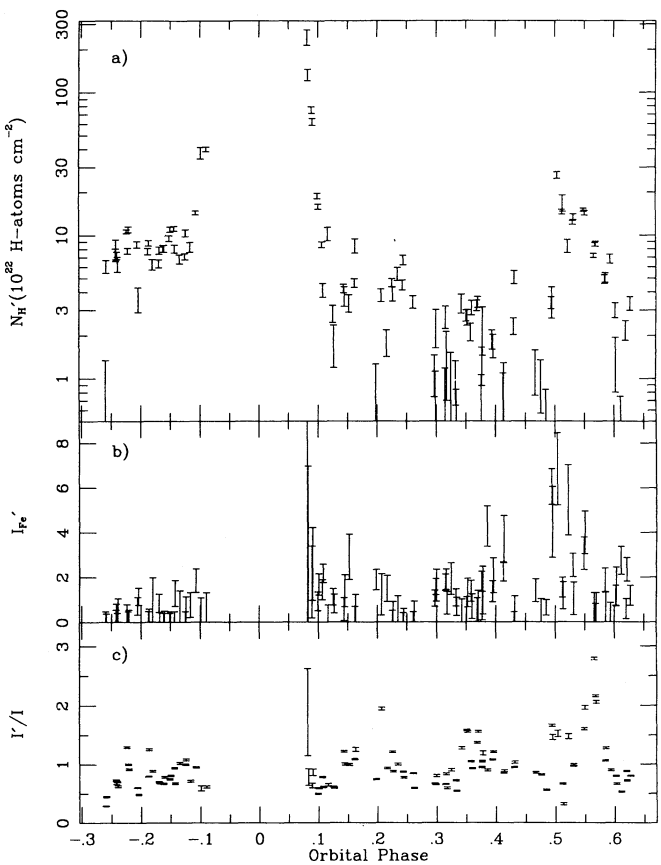

FIG. 2.—Plots of fitted quantities characterizing the X-ray spectra against orbital phase: (*a*) column density of hydrogen atoms; (*b*) iron line intensity; (*c*) intensity fluctuations relative to the synthesized average source spectra.

computed PHD obtained by convolving the LAC response matrix with a spectrum derived from the source spectrum for the interval by adjustment of the column density N'_H of cold matter, the normalization factor I'/I and the intensity I'_{Fe} of the fluorescent iron line at 6.4 keV. The other five parameters were held constant. For $\sigma(E)$ we used the absorption cross section for cold matter and reserved for later a more realistic approach that takes into account the effects of X-ray ionization of the circumsource matter. Plots of the fitted parameters against orbital phase are displayed in Figure 2: N'_H in the top panel of Figure 2, I'_{Fe} in the middle panel, and in the bottom panel the ratio I'/I, representing apparent fluctuations in the source luminosity relative to the synthesized average source spectrum.

2.2. *Variation with Orbital Phase of the Nominal Column Density*

The sharp increases of N'_H near orbital phases -0.1 and 0.1 mark the ingress and egress of the X-ray eclipse. The high values at orbital phases just before ingress and from 0.50 to 0.60 indicate the presence of circumstellar density enhancements caused by the passage of the neutron star through the wind of the primary, as simulated in the numerical computations of Blondin et al. (1990). The line of sight to the X-ray source apparently passed through these density enhancements before and during ingress. Since this effect obscures the density structure of the free-flowing wind, we first focus our attention on the data recorded during egress and later consider the effects of the density enhancements.

Figure 3 is a plot of N'_H against orbital phase during the eclipse egress. The earliest and largest value plotted is based on data from the first accumulation interval after eclipse that shows a statistically significant count rate above the eclipse level. It is plotted at orbital phase 29°.4, corresponding to the midpoint of the accumulation interval. There is a data gap preceding that interval. Considering the trends of the count rates and the values of N'_H derived from the spectrum shapes near the start of egress, we conclude that the emergence from eclipse would have been detected in a preceding accumulation interval if there had not been a data gap. We therefore put the start of egress at orbit phase 28°.3 ± 0°.5.

To interpret our egress data in terms of the distribution of matter in the free-flowing wind, we represent the number density of hydrogen atoms at the distance r from the center of QV Nor by the function

$$n(r) = \frac{\Psi}{4\pi\mu r^2}\left[1 + \left(\frac{r}{r_1}\right)^2\left(1 - \frac{r_0}{r}\right)^{\beta} \exp\left(-\frac{r - r_1}{h}\right)\right] \times \left(1 - \frac{r_0}{r}\right)^{-\beta}, \quad (2.2)$$

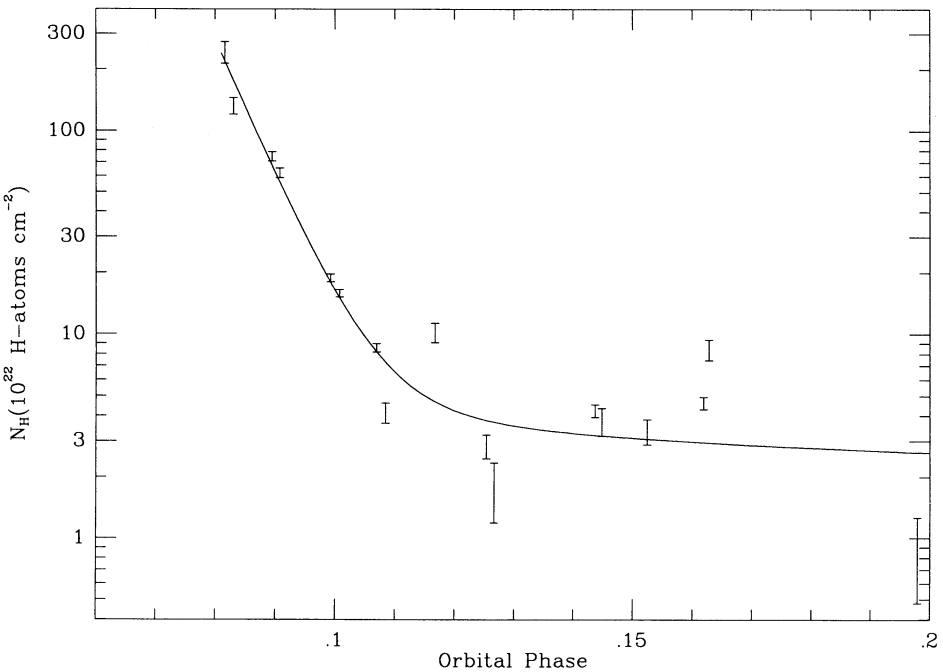

FIG. 3.—Column densities derived from the spectrum fits plotted against orbital phase, together with the fitted curve based on the hybrid density function. The fitted parameters of the density function are listed in Table 3.

in which $\Psi = \dot{M}/v_t$ represents the ratio of the mass-loss rate to the terminal velocity of the wind. The quantity r_0 is an effective radius of QV Nor that we set equal to the value 0.97×10^{12} cm implied by the eclipse angle of 28°.3 and the binary system parameters listed in Table 1. The exponent β is constrained to values ≥ 0. This density function is a hybrid formed by mating an exponential and a power law with parameters h, β, and r_1, which can be adjusted so that the function conforms to an exponential near the stellar surface and to the power law at large distances. With $r_1 < r_0$ and $h \ll r_0$ the hybrid function conforms all the way to the density function implied by the velocity law of equation (1.1). With $\beta = 0$ the function is an exponential near the surface and approaches the density of a constant-velocity wind. The velocity functions corresponding to these particular cases are illustrated in Figure 4.

We integrated the density function along the various lines of sight corresponding to the orbital phase of the midpoints of each integration interval to obtain values of the predicted column densities which were fitted to the data by adjustment of the parameters Ψ, r_1, h, and β. The fitted curve of column density is plotted against orbital phase in Figure 3, and the fitted values of the hybrid density function parameters are listed in Table 3. The best fit was obtained with $\beta = 0$. Thus the fitted density function is an exponential near the stellar surface with a slow initial acceleration, unlike the power-law density function of equation (1.1). Beyond $r \approx r_1 = 1.4r_0$ the fitted function approaches the $1/r^2$ law of a constant-velocity wind.

2.3. *Global Fit of the Density Function to the Egress Spectra Using Photoelectric Cross Sections of X-Ray–ionized Matter*

The above analysis of the variation of the column density is deficient in its neglect of the effects of X-ray ionization and heating on the absorption cross sections of the material through which the X-rays pass. To remedy this, we sought a density model in the form of equation (2.2) that yields a global fit of calculated PHDs, derived from the nominal source spectra, to all 16 of the accumulated PHDs from the period of the eclipse egress. We computed the effects of X-ray ionization and heating on the absorption cross sections according to the XSTAR code based on theoretical work of Kallman &

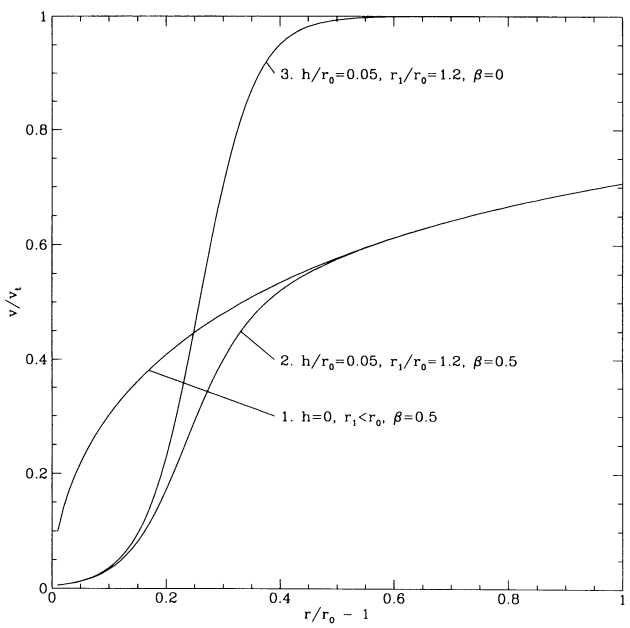

FIG. 4.—Plots of the velocity functions implied by the hybrid density function, eq. (2.2), for three sets of parameter values. All three curves are normalized to the same terminal velocity. Curve 1 is the velocity curve of eq. (1.1) with $\beta = 0.5$. Curve 2 conforms to the velocity curve implied by a density function that is an exponential near the stellar surface and a power law with $\beta = 0.5$ beyond $r \approx 1.4r_0$. Curve 3 corresponds to a density function that is exponential near the stellar surface and approaches the $1/r^2$ law of a constant-velocity wind beyond $r \approx 1.4r_0$.

TABLE 3

SUMMARY OF FITTED DENSITY FUNCTION PARAMETERS[a]

Parameter	Column Density Fit	Global Spectra Fit
$\Psi(10^{-9}\,M_\odot\,\mathrm{yr}^{-1}\,\mathrm{km}^{-1}\,\mathrm{s})$	0.23	0.67
$r_0(10^{12}\,\mathrm{cm})$	(0.97)	(0.97)
β	0.44	0.0
$h(10^{12}\,\mathrm{cm})$	0.045	0.043
$r_1(10^{12}\,\mathrm{cm})$	1.27	1.22
$N_{\mathrm{H}}^{\mathrm{ISM}}(10^{22}\,\mathrm{cm}^{-2})$	(1.6)	(1.6)
χ_ν^2	17.8	4.6
Degrees of freedom	48	316
Fitted parameters	4	4

[a] Parenthesized quantities were held constant.

McCray (1982) and Krolik & Kallman (1984) and kindly given to us by T. Kallman (1992, private communication). The code computes the absorption cross sections for matter with normal cosmic abundances under the assumption of local thermal and ionization equilibrium for a wide range of conditions of density and X-ray illumination in the approximation of one-dimensional forward propagation. It yields the absorption cross section $\sigma(\xi, E)$ as a function of energy E for a specified X-ray spectrum and a range of densities and X-ray intensities characterized by the ionization parameter

$$\xi = \frac{L_x}{nd^2}, \tag{2.3}$$

where L_X is the X-ray luminosity of the source in the energy range from 13.6 eV to 13.6 keV, d is the distance from the source, and n is the local particle number density. With the XSTAR code we computed the photoelectric cross sections for various ionization parameters as shown in Figure 5. To illustrate the effect of X-ray ionization on the propagation of an X-ray spectrum through matter near the X-ray source, we computed the attenuation of a simple power-law spectrum after passage through a column density of 1×10^{22} H atoms cm^{-2} with $\log \xi = 0.0$ and 2.0. The emergent spectra are shown in Figure 6, where the greater transparency of the ionized matter below 3 keV is evident.

We fitted calculated PHDs simultaneously to all 16 PHDs recorded in channels 8–27 during the egress by adjusting the four parameters of the hybrid function of equation (2.2) with $\beta \geq 0$ as before. For this global fitting procedure we employed an iterative least-squares code that starts each successive iteration with the 16 nominal source spectra and propagates each one step by step through the atmosphere along the line of sight, computing at each step the absorption according to the cross section for the local value of the ionization parameter. The latter depends on the local flux of X-rays, which depends, in turn, on the amount of attenuation that has occurred up to that point. We assumed that the initial value of L_X/d^2 was $3.0 \times 10^{36}/d^2$ ergs s^{-1}. At each step we evaluated ξ from the local attenuated value of L_X/d^2, and derived the local absorption cross sections by interpolation of the data displayed in Figure 5. Beyond 20 stellar radii an additional interstellar attenuation was computed for a constant column density of 1.6×10^{22} H atoms cm^{-2} of cold matter. The final attenuated spectrum for each data-accumulation interval was convolved with the LAC response matrix to obtain a trial PHD that was compared with the data to compute improved values of the density function parameters to be used in the next iteration.

Figure 7 shows the global fit obtained with the parameters listed in Table 3. Since the procedure by which we compensate for intrinsic intensity fluctuations is not exact, we cannot expect to achieve a reduced χ^2 with a value of ~ 1.0. As in the fit of the density function to the nominal column densities without ionization, the best global fit is achieved with $\beta = 0$.

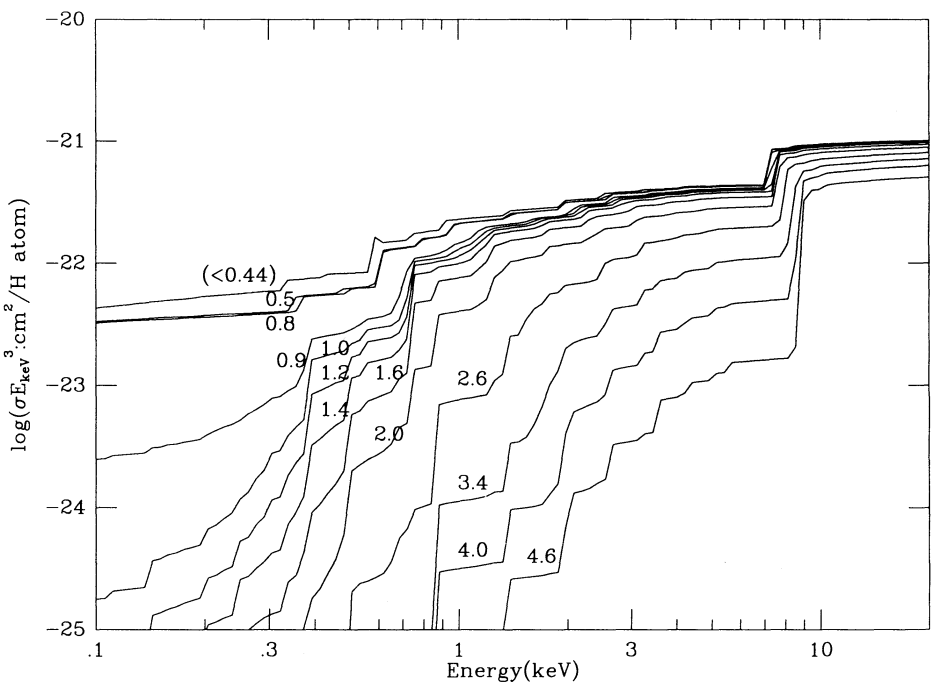

FIG. 5.—Photoelectric absorption cross sections computed by the XSTAR code for various values of log ξ

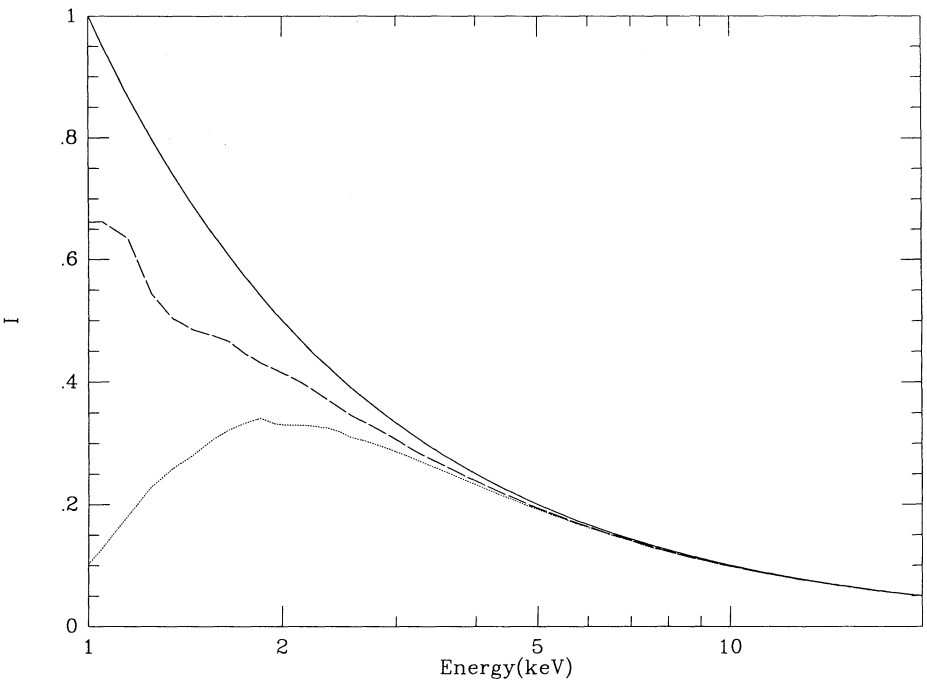

FIG. 6.—Comparison of the attenuation of a power-law spectrum by passage through a column density of 1×10^{22} H atoms cm^{-2} with values of log ζ equal to 0.0 (*dotted line*) and 2.0 (*dashed line*). The solid line represents the unattenuated spectrum.

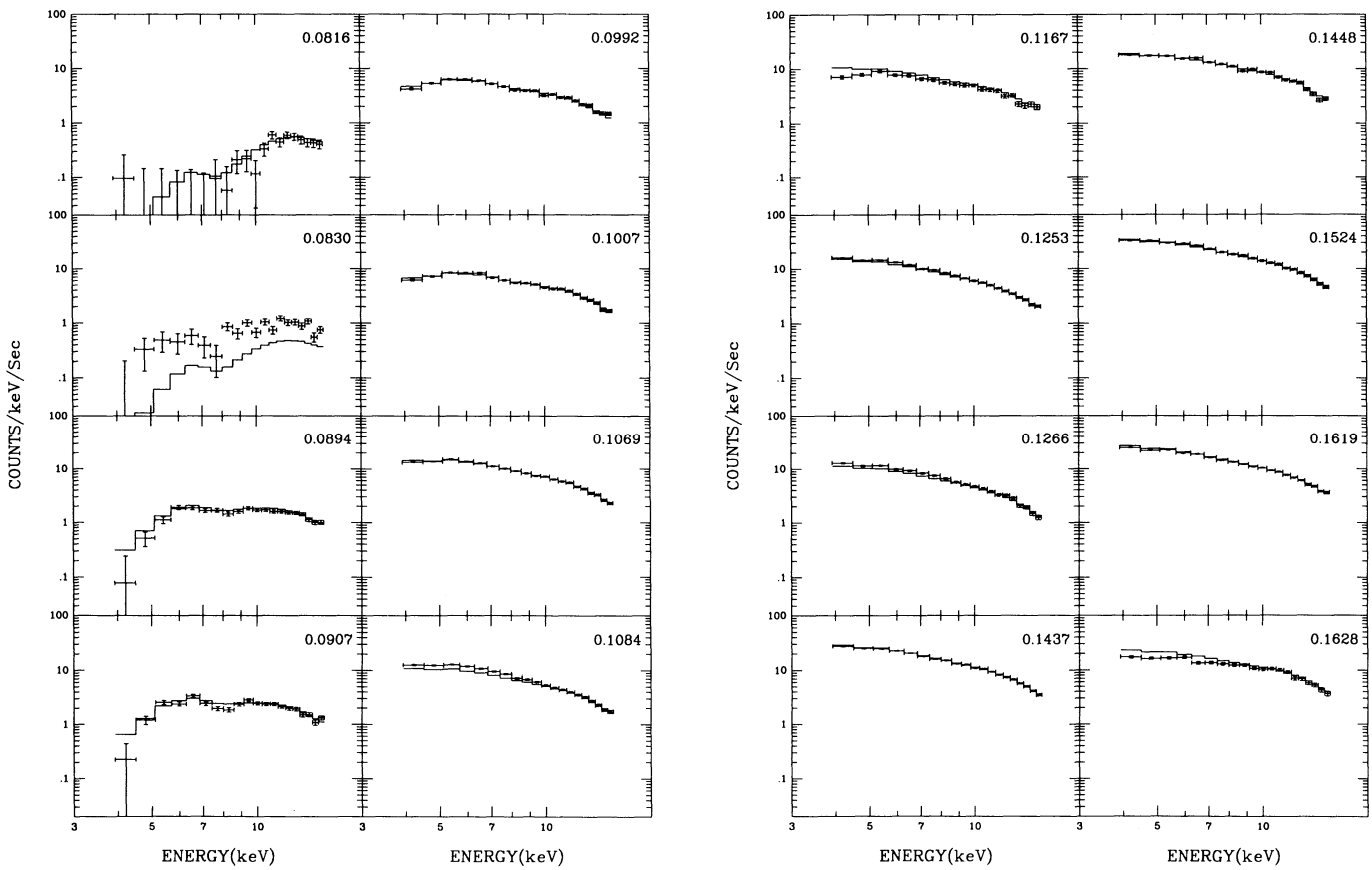

FIG. 7.—Global fits of calculated PHDs derived from the hybrid density function

Thus the fitted density functions in both cases have the form

$$n(r) = \frac{\Psi}{4\pi\mu r^2}\left[1 + \left(\frac{r}{r_1}\right)^2 \exp\left(-\frac{r - r_1}{h}\right)\right], \qquad (2.4)$$

which conforms to the exponential factor in the region $r < r_1$, and to $1/r^2$ beyond r_1. The principal difference between the fitted function from this analysis and the previous one is the larger value of Ψ that is required to compensate for the reduced absorption cross sections of ionized matter.

Figure 8 displays contours of constant log ξ in the wind described by the globally fitted density function and irradiated by X-rays emitted by the source with the intrinsic source spectrum derived from the averaged uneclipsed low-attenuation PHD. The lines of sight at the midpoints of each of the 16 accumulation intervals during egress are shown as straight lines, four of which appear in projection on the stellar disk at the assumed inclination angle.

2.4. *Monte Carlo Computation of X-Ray Propagation*

To obtain a prediction of the spectrum of X-rays emerging from the system in any specified direction and, in particular, into the eclipse shadow, we developed a Monte Carlo code to compute the propagation of X-rays in three dimensions through an X-ray–ionized atmosphere. We assumed initially that the density in the atmosphere is given by the globally fitted density function and the distribution of the ionization parameter values displayed in Figure 8. The code employs the absorption cross sections displayed in Figure 5, and it takes account of Compton scattering, photoelectric absorption, and fluorescent emission from iron and lower Z elements with normal cosmic abundances. The code launches X-ray photons of a specified energy from the neutron star in directions uniformly distributed among $\sim 10^4$ equal $2° \times 2°$ elements of solid angle over the entire sphere. Each photon is tracked in steps of one-tenth or less of a mean interaction length. At each step a photon has a chance to suffer a Compton scattering resulting in a change of direction and a small reduction in energy, or a photoelectric absorption with the possible emission of a fluorescent X-ray photon. The code tabulates the exit direction and energies of the photons in the same $\sim 10^4$ elements of solid angle. The resulting tabulations constitute, in effect, a transfer matrix to map a given spectrum of X-rays emitted isotropically by the neutron star into the spectrum of transmitted and scattered X-rays that would be observed at a distant point in any given direction. A run consisted of 500 photons at each of 40 energies from 0 to 70 keV in each of the $\sim 10^4$ directions.

Figure 9 displays the results of the Monte Carlo computation for 3 keV and 10 keV X-rays. The solid lines trace the fractional yield of scattered X-rays as a function of orbital phase at an inclination angle of 70°. The dashed lines in the 10 keV plot shows the fractional yield of iron fluorescent X-rays. The plots show that the X-ray albedo of the primary star due to source photons of 10 keV is about 4% in the range of orbital phase ($\phi = 0.28$–0.45) from which we took our low-attenuation data.

The average PHD recorded during the eclipse in the orbital phase interval from -0.067 to $+0.067$ is displayed in Figure 10. The X-ray energy flux observed is about 10^{-4} times the

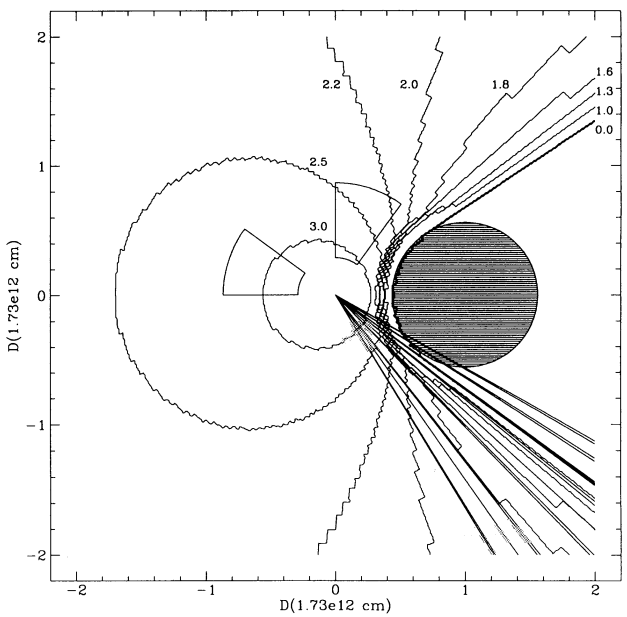

FIG. 8.—Ionization contours for the fitted hybrid density function and a source luminosity of 3×10^{36} ergs s^{-1} in the energy range below 13.6 keV. The wrinkles in the contour lines are an artifact of the computation. The numbers are the values of log ξ. The lines of sight at the midpoints of each of the intervals for accumulation of the data used in the global fit are indicated by the lines emanating from the source. The intersection pattern of the density enhancement in the orbital plane is shown as the two paddle-shaped figures.

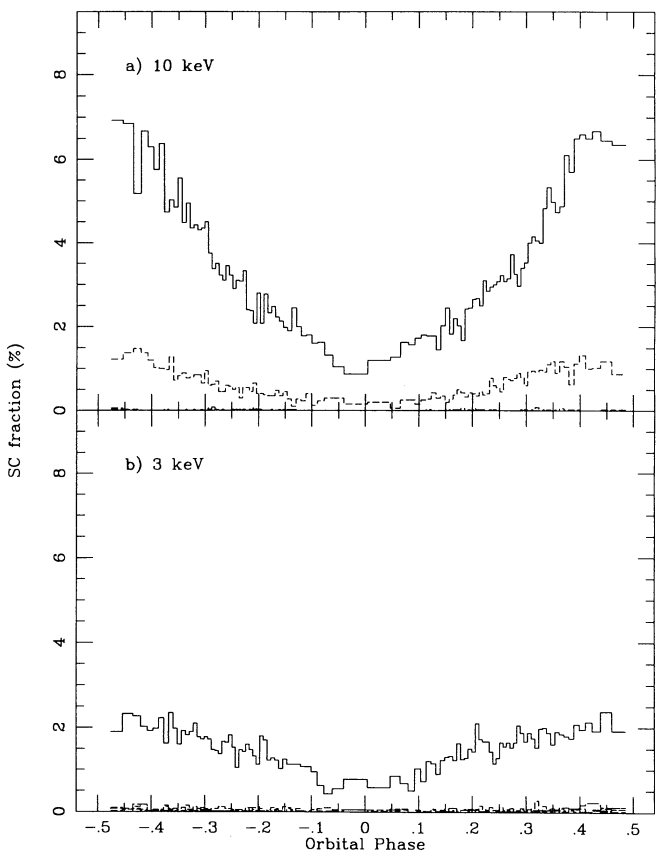

FIG. 9.—Compton-scattered (*solid curves*) and fluorescent (*dashed curves*) fractions of X-rays for (*a*) 10 keV and (*b*) 3 keV plotted against orbital phase as derived from the results of the Monte Carlo computation. The upper dashed curve in (*a*) is for K-line fluorescence of iron. The lower dashed curves (barely visible) are for K-line fluorescence of the lighter elements.

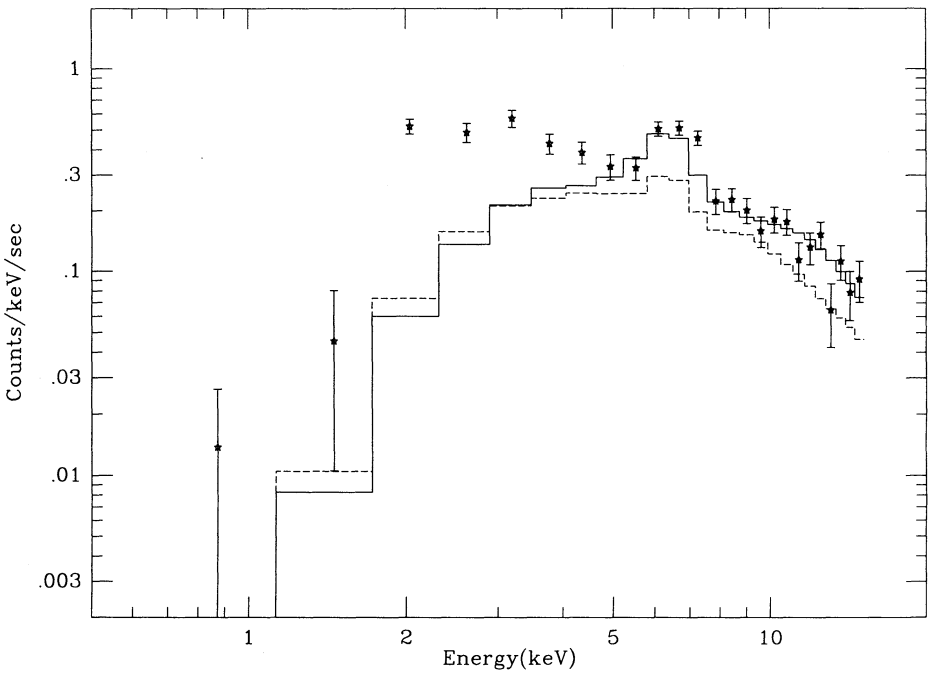

FIG. 10.—Average PHD recorded during eclipse. The dashed line is the PHD predicted by Monte Carlo computation for X-rays with the intrinsic source spectrum that have been scattered from circumstellar matter with the hybrid density function derived in the global fit of the egress data, and reduced by interstellar attenuation. The solid line is the predicted PHD obtained with a density enhancement equivalent in effect to an increase in the wind parameter Ψ by a factor of 1.33. The difference between the observed PHD and the normalized Monte Carlo prediction below 4.5 keV is the "soft component" of the eclipse spectrum.

bolometric flux of the primary, QV Nor, which is two orders of magnitude larger than the L_X/L_{bol} ratios typical of O and B0 supergiants (Cassinelli et al. 1981). We have assumed, therefore, that the contribution of coronal X-rays to the eclipse spectrum is negligible. We applied the Monte Carlo–derived transfer matrix to the average uneclipsed source spectrum to predict the average deep eclipse spectrum recorded between orbit phases -0.067 and $+0.067$. The resulting spectrum was reduced by interstellar attenuation in cold matter with $N_H = 1.6 \times 10^{22}$ H atoms cm^{-2}, and then convolved with the LAC response matrix to obtain the predicted PHD of X-rays scattered into the umbra. The latter is shown as the dashed line in Figure 10. Above channel 9 (5.1 keV) it is similar in form to the observed distribution, but only about two-thirds of the observed count rate. We attribute the remaining third to X-rays scattered from the density enhancements whose existence is indicated by the episodes of strong absorption in the uneclipsed spectra.

The enhancements, attributable to an accretion wake, are sources of additional Compton-scattered intensity, as well as likely sources of thermal X-rays from shock-heated gas. To model their contribution to the scattered intensity, we added matter in a configuration suggested by the hydrodynamic calculations of Blondin et al. (1990). We chose a configuration that (1) intersects the orbital plane in a pattern that resembles the nonsteady density patterns displayed by Blondin et al., (2) yields predicted curves of count rates versus orbital phase at various energies that resemble the light curves observed as shown in Figure 11, and (3) predicts a deep eclipse PHD that conforms in shape and magnitude with the observed eclipse PHD in channels 8–27. The plot of hardness ratio in Figure 11 (*bottom panel*) indicates that the intensity minima at orbital phases -0.20 and $+0.55$ are caused by absorption, while the other intensity fluctuations are flares intrinsic to the source. The pattern of the density enhancements in the orbital plane is indicated in Figure 8, and the resulting predicted deep eclipse spectrum is shown as a solid line in Figure 10.

In channels 8 and below, the Monte Carlo calculation with the density enhancements predicts rates that are substantially smaller than the observed rates. By subtracting the Monte Carlo rates, we obtain the average PHD of what we call the "soft component" shown in Figure 12. We assume it is a mixture of delayed X-rays from the eclipsed source that have been scattered by interstellar grains, and direct X-rays emitted by hot, uneclipsed matter in the density enhancements previously described. Figure 13 displays a plot against orbital phase of the intensity of this soft component in channels 3–8 in a sequence of 18 equal phase intervals during the eclipse. The indicated errors are due primarily to the uncertainties in the background subtraction. There appears to be a downward trend during the first half of the eclipse, which may reflect the decaying intensity of grain-scattered X-rays. Sudden increases near phases -0.09, 0.01, and 0.06 may be Compton-scattered flares. The solid lines are the predicted count rates of the grain-scattered component for various grain models as described below.

3. DISCUSSION

3.1. *Properties of the Radiatively Driven Wind*

The exponential form of the density function in the low-velocity region of the wind of QV Nor, as well as in the winds of the primaries of Cen X-3 and Vela X-1, may be an important clue to the nature of the instabilities in the driving mechanism of radiation-pressure–driven winds. Such instabilities (Lucy & Solomon 1970; Nelson & Hearn 1978; MacGregor, Hartmann, & Raymond 1979; Lucy & White 1980; Lucy 1982, 1984; Owocki & Rybicki 1984; Krolik & Raymond 1985) cause turbulence and localized shock heating, which is con-

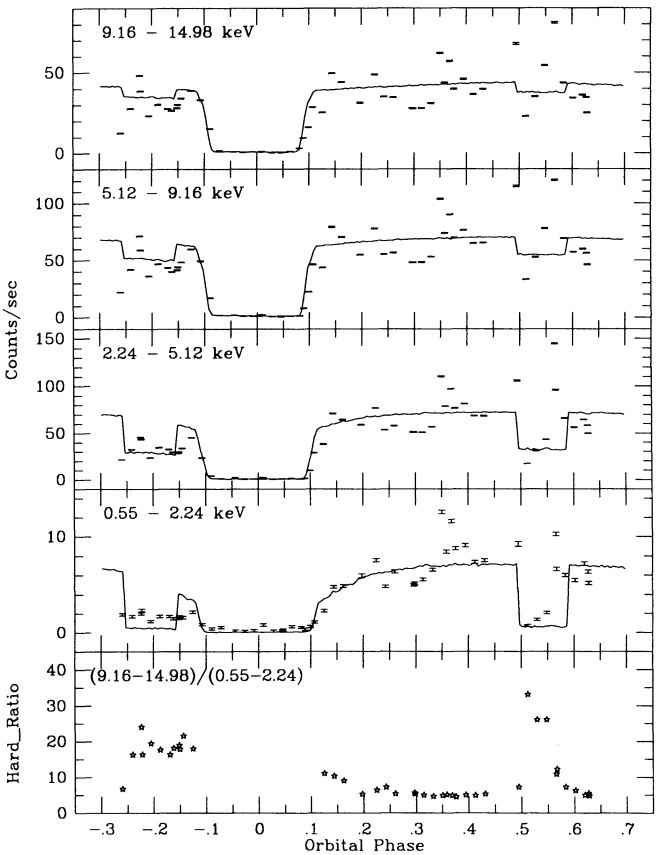

FIG. 11.—Count rates in various pulse-height channels and hardness ratio plotted against orbital phase. The nominal energy boundaries of the pulse-height channels are indicated. The solid line is the count-rate "light curve" predicted by the Monte Carlo calculation with the ad hoc density enhancements, the conspicuous effects of which are the minima around orbital phases −0.2 and +0.55.

sidered the likely source of the ubiquitous soft X-ray emission of early-type stars. Thus, the density function one derives from X-ray eclipse transition data must be an average over an inherently nonsteady density distribution.

Poe, Owocki, & Castor (1990) explored the solution topology of an equation describing the acceleration of a radiatively driven wind without the Sobolev approximation. They find that the solutions are intrinsically unstable for realistic values of v_{th}/v_a, the ratio of the ion thermal speed to the sound speed. By setting this ratio to the unrealistic value 0.5, they obtain a stable solution for a star of radius 1.4×10^{12} cm, which they find "corresponds to the asymptotic state approached for unperturbed models in the time-dependent simulations." They suggest that real absorption-line–driven winds, more realistically modeled with $v_{th}/v_a = 0.375$, are highly variable, "with both the velocity law and mass-loss rate fluctuating about the allowed steady values" (obtained with $v_{th}/v_a = 0.5$). Their non-Sobolev steady state solution can be fitted rather well by an exponential density function in the lower region with a scale height of 5×10^{10} cm, with a transition near $1.3r_0$ to a power-law density function with $\beta = 0.5$, and a mass-loss rate $1 \times 10^{-6}\ M_\odot\ \mathrm{yr}^{-1}$. The similarity in form of their asymptotic density curve and the one we fitted to the eclipse egress data of 4U 1538−52 lends credibility to an interpretation of our hybrid density function as an average of a turbulent flow. One might achieve a more significant comparison of the theory of unstable flow with X-ray measurements of column density profiles by computing the average density function of many randomized numerical hydrodynamic simulations of unstable flow with $v_{th}/v_a = 0.375$.

For the purpose of testing the theory of radiation-driven winds, Abbott (1982) summarized the correlations between terminal wind velocity and escape velocity, and between mass-loss rate and luminosity, as derived from radio and UV measurements of early-type stars. To compare our results with those correlations, we first estimate the escape velocity according to the formula. $v_{esc} = [2GM(1-\Gamma)/r_0]^{1/2}$, where Γ is the ratio of the optical luminosity to the Eddington luminosity. For the mass ratio $M_{opt}/M_x = 16.1 \pm 1.2$ and luminosity $L = 10^{5.21\pm0.13}\ L_\odot$ given by Reynolds, Bell, & Hilditch (1992), the radius $r_0 = 0.97 \times 10^{12}$ cm we derived, and a neutron star mass of $1.4\ M_\odot$, the escape velocity is $(6.9 \pm 0.5) \times 10^2$ km s^{-1}. In Abbott's correlation plot stars of luminosity class I with this escape velocity have terminal velocities in the range (1.4–2.8) $\times 10^3$ km s^{-1}. The mass-loss rate implied by our global fitted value of $\Psi = \dot{M}/v_t$ for this range of terminal velocities is in the range (0.9–1.9) $\times 10^{-6}\ M_\odot\ \mathrm{yr}^{-1}$. According to Abbott's other correlation plot, stars with luminosities in the range of QV Nor have mass-loss rates in the range (0.03–1.0) $\times 10^{-6}$ $M_\odot\ \mathrm{yr}^{-1}$. Thus the mass-loss rate we have derived from X-ray eclipse data for QV Nor is on the upper fringe of values found for stars of the same luminosity from radio and UV data.

3.2. *Origin of the Soft Excess Observed out of Eclipse*

The density enhancements we have invoked to boost the predicted Compton-scattered spectrum in eclipse are like those seen in the simulations of Blondin et al. (1990), in which radiation-pressure–driven wind moving with high velocity piles up against coasting X-ray–ionized plasma. The solid curve in Figure 12 is the PHD of a thermal bremsstrahlung spectrum fitted to the data by adjustment of the intensity and the temperature. The fitted value of the temperature is 9×10^6 K, and the fitted intensity, if isotropic, implies a luminosity of 9×10^{33} ergs s^{-1} in the 1–10 keV band at 5.5 kpc.

One would expect the density enhancements that result from the pileup to be shock-heated to a temperature $\sim 3\mu v_s^2/16k \sim 3.0 \times 10^7 (v_s/1000\ \mathrm{km\ s^{-1}})^2$ K, where v_s is the upstream velocity (McKee & Hollenbach 1980). The luminosity of a wind with a mass-loss rate and terminal velocity in the ranges estimated for QV Nor in § 3.1 would lie in the range from 6×10^{35} to 5×10^{36} ergs s^{-1}, so the interception and conversion of only a small fraction of the wind energy would be sufficient to generate the observed soft X-ray component. Thermal emission from the density enhancements is therefore a plausible source of the soft component.

3.3. *Properties of Interstellar Grains Inferred from a Comparison of X-Ray Scattering and Optical Extinction*

Our goal here is to derive a constraint on models of interstellar grains, i.e., on their composition and size distribution, from a comparison of the intensity of grain-scattered X-rays from 4U 1538−52 during its eclipse with the optical extinction of its companion QV Nor. In the analysis similar to that of Kitamoto, Miyamoto, & Yamamoto (1989), we seek to evaluate or limit the quantity $R_{XV}(E)$, which we call the scattering/extinction ratio of a grain model. We define $R_{XV}(E)$ as $(E/1\ \mathrm{keV})^2$ times the quotient of the optical depth for scattering X-rays of energy E by the optical extinction at wavelength 5550 Å.

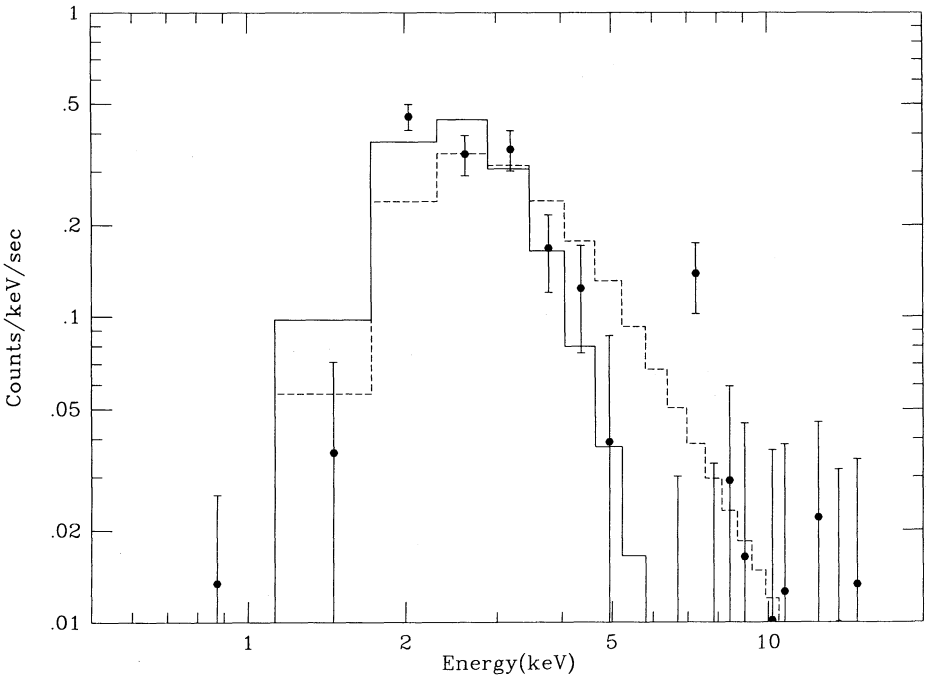

FIG. 12.—Pulse-height distribution of the soft component derived by subtracting the Monte Carlo distribution from the average eclipse distribution. The solid line is the predicted distribution that might be attributed to thermal bremsstrahlung from optically thin plasma at a temperature of 5×10^6 K and a source luminosity of 5.3×10^{34} ergs s^{-1} in the energy range from 1 to 10 keV. The dashed line is the predicted spectrum of grain-scattered X-rays adjusted in amplitude to fit the data.

For a given model of grains with an assumed uniform density along the line of sight, the optical depth for scattering is

$$\tau(E) = \pi D \int Q_{\rm scat}(x_E) a^2 n_g(a) da \,, \tag{3.1}$$

where D is the distance of the source, $Q_{\rm scat}(x_E)$ is the scattering efficiency of grains of radius a for X-rays of energy E, $x_E = 2\pi aE/hc$, $n_g(a)da$ is the density of grains with radius a in da, and h and c are Planck's constant and the speed of light, respectively. The total optical extinction in magnitudes caused by the same population of grains is

$$A_V = 1.086\pi D \int Q_{\rm ext}(x_V) a^2 n_g(a) da \,, \tag{3.2}$$

where $Q_{\rm ext}(x_V)$ is the extinction efficiency and $x_V = 2\pi a/\lambda_V$, with $\lambda_V = 5500$ Å (Spitzer 1978). Thus the scattering/extinction ratio is

$$R_{XV}(E) = \left(\frac{E}{1\ \rm keV}\right)^2 \frac{\tau(E)}{A_V} = \left(\frac{E}{1\ \rm keV}\right)^2 \frac{\int Q_{\rm scat}(x_E) a^2 n_g(a) da}{1.086 \int Q_{\rm ext}(x_V) a^2 n_g(a) da} \ \rm mag^{-1} \,, \tag{3.3}$$

a quantity that can be computed for a given grain model.

In the Rayleigh-Gans approximation the scattering efficiency of a spherical particle of radius a for X-rays of energy E is (van de Hulst 1981).

$$Q_{\rm scat}(x_E) = 2(r_e n_e hca)^2 E^{-2} \,, \tag{3.4}$$

where n_e is the electron density in the grain and r_e is the electron radius. In terms of the specific density ρ, the mean mass number M, and the mean atomic number Z, the electron density is $n_e = \rho(Z/M)N_A$, where N_A is Avogadro's number. The approximation is valid for $a(\rho/E) < 0.5$ μm, where E is in units of 1 keV. The counts we attribute to the soft component of the eclipse spectrum are concentrated in the channels corresponding to energies in the range $\sim$2–4 keV. We can therefore use the Rayleigh-Gans approximation for grains with radii less

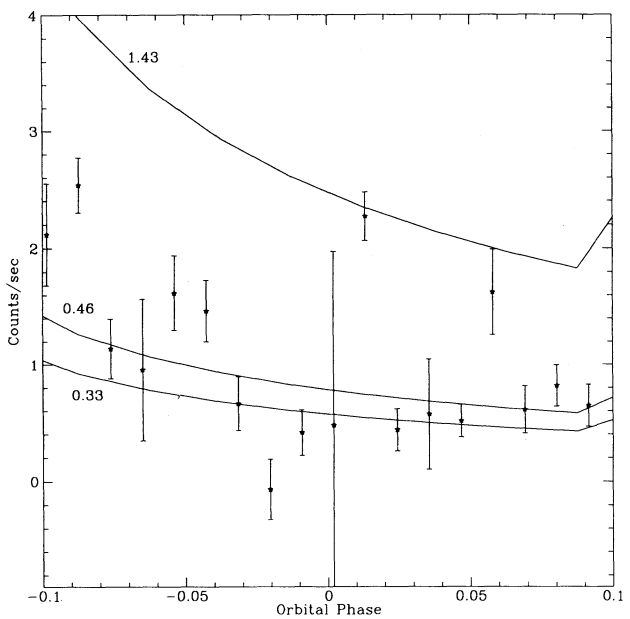

FIG. 13.—Plot of the soft component count rate in successive equal intervals of orbital phase against orbital phase during the eclipse. The curves are the predicted rates for grain-scattered X-rays based on the previous history of the source intensity out of eclipse and the indicated values of k_g for three grain models computed from the data of Martin & Rouleau (1991): "astronomical silicate" ($k_g = 1.43$); graphite ($k_g = 0.33$); and a silicate-graphite mixture ($k_g = 0.46$).

than $\sim 1.0/\rho$ μm. Combining equations (3.3) and (3.4), evaluating the constants, and expressing a in units of 0.1 μm, we obtain for the scattering/extinction ratio in the Rayleigh-Gans approximation the energy-independent expression

$$R_{XV} = 0.184\left(\frac{2Z}{M}\right)^2\left(\frac{\rho}{3}\right)^2 \times \int a^4 n_g(a)da \Big/ \int Q_{ext}(\chi_V)a^2 n_g(a)da \text{ mag}^{-1} . \quad (3.5)$$

Turning to an analysis of the data that constrain this constant, we call $I_g(E, t)$ the intensity of grain-scattered X-ray photons of energy E in the halo of an image of the source at time t, and $I_C(E, t')$ the pulse-phase–averaged intensity of the unscattered X-rays in the image core at an earlier time $t' < t$. Representing the source intensity that would have been observed in the absence of scattering as $I_C(E, t')$ exp $\tau(E)$, and assuming that the core and halo components have suffered the same interstellar absorption, we can express the grain-scattered intensity as

$$I_g(E, t) = \frac{\exp \tau(E) - 1}{\tau(E)} \int_{-\infty}^{t} I_C(E, t') \times \left[\pi D \int Q_{scat}(x_E)a^2 n_g(a)P(E, a, t'')da\right]dt' , \quad (3.6)$$

where $P(E, a, t'')$ is the probability distribution of delay times $t'' = t - t'$ of photons with energy E that have been scattered by grains of radius a. Combining equations (3.2), (3.3), and (3.6), we obtain

$$I_g(E, t) = A_V R_{XV}\left(\frac{E}{\text{keV}}\right)^{-2} \frac{\exp \tau(E) - 1}{\tau(E)} \int_{-\infty}^{t} I_C(E, t') \times \left[\int a^4 n_g(a)P(E, a, t'')da\right]dt' \Big/ \int a^4 n_g(a)da , \quad (3.7)$$

which is an expression for the expected grain-scattered halo intensity in terms of the unscattered core intensity at earlier times, the optical extinction, and the grain model as expressed in the scattering and extinction efficiencies and the grain-size distribution. A comparison of the observed grain-scattered intensity with the expected intensity computed according to equation (3.7) provides a test of the model. To facilitate such a comparison, we will put equation (3.7) into a more useful, approximate form.

Lacking image data, we have no way to distinguish directly between the halo and core components of the measured intensities. To proceed, we take advantage of the smallness of $\tau(E)$ in the energy range of interest, $E > 1.5$ keV, and adopt the following approximations:

1. $\{[\exp \tau(E) - 1]/\tau(E)\}I_C(E, t') \approx I(E, t')$, the total intensity measured at t'.
2. $P(E, a, t'') \approx P_1(E, a, t'')$, which we call the probability distribution of the delays suffered by photons that arrive after only a single scattering.

Alcock & Hatchett (1978) derived the distribution in delay of X-rays scattered by grains distributed uniformly along the path from source to observer, and provided an approximate formula that fits the theoretical delay distribution of singly scattered photons. Their formula for the probability per unit time of a photon arriving with a delay equal to t'' can be written as

$$P_1(E, a, t'') = [0.86 \exp(-t''/t_g) + 0.64 \exp(-6.8t''/t_g)]/t_g , \quad (3.8)$$

where

$$t_g = 0.71\left(\frac{hc}{2\pi aE}\right)^2 \frac{D}{2c} \approx 40\left(\frac{a}{0.1\ \mu\text{m}}\right)^{-2}\left(\frac{E}{1\ \text{keV}}\right)^{-2}\left(\frac{D}{1\ \text{kpc}}\right) \text{hr} . \quad (3.9)$$

We represent the grain-size distribution by the formula of Mathis, Rumpl, & Nordsieck (1977, hereafter MRN):

$$n_g(a) \sim a^{-p} , \quad a_1 < a < a_2 . \quad (3.10)$$

In our earlier analysis of the variation of the spectrum with orbital phase, we represented the spectrum measured at a given orbital phase as a product of a constant spectrum, derived from the low-attenuation portion of the orbital phase, times a variable attenuation factor, i.e.,

$$I(E, \phi) = I_0(E) \exp[-\sigma(E)N_H(\phi)] , \quad (3.11)$$

in which $N_H(\phi)$ is the column density at orbit phase ϕ, as displayed in Figure 2*a*. Our observations extended over $\sim 90\%$ of one orbital period of the binary, starting about 18 hr (0.2 period) before the eclipse ingress. To extend the time integral in equation (3.5) to times before our observations began, we will assume that $N_H(t')$ was a periodic function of phase over several orbital periods prior to and including the times of our observation. We represent this periodic function as a sequence of the averages in equal 0.025 phase intervals of the values of N_H plotted in Figure 2*a*, and fill in the missing data with a linear interpolation in the phase interval 0.65–0.75.

We now rewrite equation (3.7) as

$$I_g(E, t) = k_g I_0(E)\left(\frac{E}{1\ \text{keV}}\right)^{-2} G(E, t) , \quad (3.12)$$

where

$$G(E, t) = \frac{5 - p}{a_2^{5-p} - a_1^{5-p}} \int_{-\infty}^{t} \exp[-\sigma(E)N_H(\phi')] \times \left[\int_{a_1}^{a_2} a^{4-p} P_1\left(\frac{t''}{t_g}\right)da\right]dt' , \quad (3.13)$$

and

$$k_g = A_V R_{XV} . \quad (3.14)$$

In equation (3.13), ϕ' represents the orbital phase of the binary system at the time t', and $t'' = t - t'$. We note that if N_H is constant, then $G = \exp[-\sigma(E)N_H]$, and $R_{XV} = (E/1\ \text{keV})^2(I_g/I)A_V^{-1}$ mag^{-1}, where I_g/I represents the fractional halo intensity at energy E.

Displayed in Figure 14 are plots of $I_g(E, \phi)/k_g$ against orbital phase for several values of E in the range 1–5 keV, and a grain-size distribution specified by the MNR power law with $a_1 = 0.005$ μm, $a_2 = 0.25$ μm, and $p = 3.5$. They show the excursions in halo intensity caused by the orbital phase-dependent variations in the amount of absorption in the source spectrum, including, of course, the energy-dependent decays that follows the eclipse ingress. We note, in particular, that the high pre-eclipse absorption ($-0.25 < \phi < -0.10$) strongly depresses the intensity in the 2–4 keV range which produces most of the counts recorded during the eclipse.

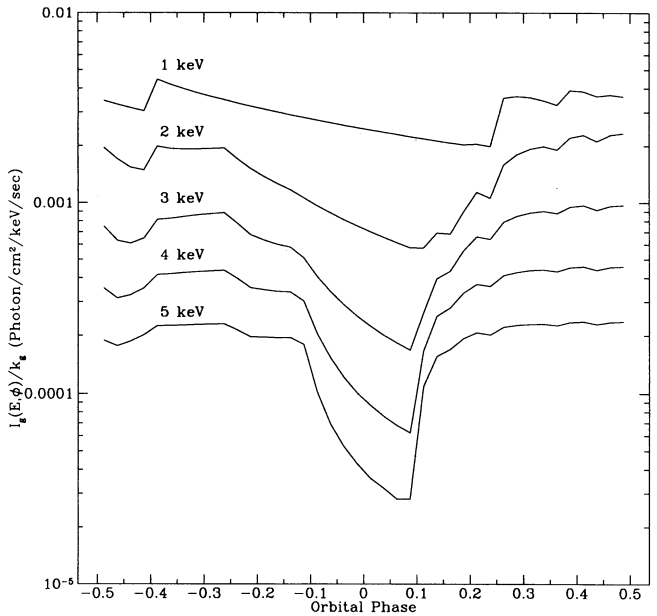

FIG. 14.—Plots of $I_g(E, t)/k_g$ against orbital phase for several values of E in the range 5 keV.

We convolved the predicted grain-scattered spectrum of equation (3.12) with the LAC response matrix to obtain predicted PHDs, which we sum from channels 3 through 8 for comparison with the rates of the soft component actually observed during the eclipse. Curves of the predicted rates for several values of k_g are plotted as solid lines in Figure 13.

Thermal X-rays from uneclipsed shocked circumsource matter must comprise some portion of the soft component in eclipse. Nevertheless, the downward trend in the rate of the observed soft component in the first half of the eclipse is the expected behavior of the grain-scattered component. Discounting the flarelike high values, and attributing the entire nonflare soft component to grain-scattered X-rays, we find that the data are consistent with the curve for $k_g = 0.33$, and place an upper limit of $k_g < 0.4$. The corresponding upper limit on R_{XV} is 0.06 mag^{-1}.

For a comparison with previous observations of grain scattering, we turn first to the work of MG, who determined the fractional halo intensities of six X-ray stars by dissecting images recorded by the *Einstein Observatory*. They summarized their results in a plot of measured fractional halo intensities against optical extinctions, to which they fitted a straight line that does not intersect the origin as expected according to equation (3.12). Nevertheless, for $A_V = 6.5$ mag, the optical extinction of QV Nor, their linear relation predicts a fractional grain-scattered intensity of 0.12 at $E \approx 2.0$ keV. Since their observations were of uneclipsed sources and their analyses were based, in effect, on the assumption of steady state conditions for which $G(E, t) = \exp[-\sigma(E)N_H]$, their results imply $k_g \approx 0.48$ and $R_{XV} \approx 0.073$ mag^{-1}. The corresponding predicted curve would lie between the curves for $k_g = 0.33$ and 0.73 in Figure 14, slightly higher than our upper limit.

Predehl et al. (1991) dissected the grain-scattered halo of the image of GX 339−4 obtained with *ROSAT*. They found a fractional halo intensity of 0.099 at $E = 1.1$ keV, which implies $k_g = 0.12$. With $A_V \sim 3.5$ for the optical counterpart (Grindlay 1979) and the assumption of steady state conditions, these data imply $R_{XV} = 0.034$ mag^{-1}.

In *Tenma* observations of Cyg X-1, Kitamoto et al. (1989) found a "soft excess" in the spectrum during absorption dips. They concluded that the main part of this soft component could not be attributed to the halo component, and placed an upper limit of 0.15 on the grain-scattered fraction at 1 keV. With their cited value of the extinction, $A_V = 3.3$ mag, the implied value of $R_{XV}(E)$ is 0.045 mag^{-1}, consistent with our result but substantially less than the value derived from the relation of MG. In *EXOSAT* observations of Cen X-3 ($A_V =$ 4.4 mag), Day & Tennant (1991) observed a soft excess in the eclipse spectrum, of which they attributed a portion to grain-scattered X-rays. They concluded that their derived intensity is compatible with the formula of Xu et al. (1986), which implies $R_{XV}(E) = 0.125$ mag^{-1} for $a_2 = 0.25$ and $p = 3.5$, which is substantially larger than our limit. Day & Tennant describe problems in the data analysis which indicate that a substantial portion of the soft component they isolated may be thermal emission from circumstellar matter in the Cen X-3 system. Lewis et al. (1992) found no evidence in *Ginga* data on 4U 0900−40 (Vela X-1, $A_V = 2.2$ mag) of a soft time-dependent grain-scattered component in the eclipse spectrum shortly after ingress. They suggested that the strong circumsource absorption observed during ~2 days prior to the eclipse eliminated most of the scattered X-rays that would otherwise have been detected during the eclipse. It seems likely that an analysis of their data in the manner we have described would confirm that suggestion.

On the theoretical side, the most extensive computations relevant to the interpretation of our data are those of Martin & Rouleau (1991). Using data on the optical and X-ray properties of materials derived from laboratory and theoretical studies, they calculated the effective absorption and scattering cross sections of grains for an MRN size distribution with $a_1 = 0.005$ μm, $a_2 = 0.25$ μm, and $p = 3.5$, three compositions of grain material, and photon energies ranging from 1 eV to 4 keV. Substituting values read from their plots (for $\lambda = 5550$ Å and $E = 2$ keV) in our equation (3.3), we find $R_{XV}(E) = 0.22$, 0.051, and 0.11 mag^{-1} for "astronomical silicate," graphite, and a mixture of the two materials, respectively. The corresponding values of k_g for $A_V = 6.5$ mag are 1.43, 0.33, and 0.46, for which the curves in Figure 13 are plotted. Only the curve for pure graphite grains appears to be consistent with the data. However, a model of grains composed of silicates, or the more realistic mixture of silicates and graphite, could be made consistent with our upper limit on R_{XV} if the grains are modeled as loose aggregates of smaller solid particles with an average bulk density less than that of the solid material. The reason is that the X-ray scattering efficiency of an aggregate grain decreases more rapidly with its bulk density, i.e., with the proportion of vacuum within the aggregate, than does the optical extinction. Mathis & Whiffen (1989) have considered models of such grains to explain broad-band extinction data, and have calculated their extinction efficiencies as aggregates of solid particles and vacuum "particles." We note that aggregate grains with this "fluffy" nature have been found in the interplanetary dust (Bradley, Humecki, & Germani 1992).

4. SUMMARY

We have explored the implications of the eclipse phenomena of the X-ray binary 4U 1538−52/QV Nor for the stellar wind of the primary and the properties of interstellar grains. Our principal conclusions are the following:

1. The run of density in the atmosphere of QV Nor, the massive B0 I companion of 4U 1538−52, can be fitted by a density function of the form

$$n(r) = \frac{\Psi}{4\pi\mu r^2}\left[1 + \left(\frac{r}{r_1}\right)^2 \exp\left(-\frac{r - r_1}{h}\right)\right],$$

which conforms to the exponential factor in the region $r < r_1$, and to $1/r^2$ (constant wind velocity) beyond r_1. This result, like similar results obtained from eclipse observations of Cen X-3 and Vela X-1, adds to the evidence that steady state theories of radiation-pressure–driven winds do not yield an accurate description of the velocity curves in the subsonic and low supersonic regime. The density function that does fit our data must be considered as an approximate representation of the average density in an inherently turbulent flow.

2. The fitted value of $\Psi = \dot{M}/V_t$, together with an estimate of the terminal velocity V_t based on the mass and luminosity of QV Nor, implies a mass-loss rate in the range (0.9–1.9) $\times 10^{-6}$ $M_\odot$ yr^{-1}, a result on the upper fringe of values derived by other means for similar B0 I stars and compiled by Abbott (1982).

3. The pulse-height distribution (PHD) observed in eclipse corresponding to energies above 4.5 keV can be fitted by a calculated distribution derived by a Monte Carlo computation of Compton scattering and fluorescence of X-rays by circumstellar matter, with the average density described by the hybrid function plus density enhancements caused by the effects of the accretion wake on the wind flow.

4. Subtraction from the eclipse PHD of the calculated Monte Carlo PHD, normalized to the data above 4.5 keV, leaves a soft component which can be explained in part as grain-scattered X-rays that persist with decaying intensity through the eclipse due to transit time delays, and in part as thermal emission from the shock-heated circumsource density enhancements.

5. Taking the total intensity of the soft component as an upper limit on the intensity of grain-scattered X-rays during the eclipse, we derive a constraint on models of the composition and size distribution of interstellar grains. The constraint is in the form of an upper bound on a quantity we call $R_{XV}(E)$, which is a characteristic constant of a grain model defined as $(E/1\ \mathrm{keV})^2$ times the quotient of the optical depth for scattering X-rays of energy E by the optical extinction at wavelength 5550 Å. In the Rayleigh-Gans approximation for X-ray scattering, R_{XV} is independent of the X-ray energy. Assuming that all of the soft component observed during the eclipse of 4U 1538−52 is grain-scattered, we find $R_{XV} < 0.06$ mag^{-1}. This limit is consistent with the results of a previous grain-scattering study based on dissection of the halo and core components of images obtained with *ROSAT* (Predehl et al. 1991) and marginally consistent with an earlier image-dissection study of images from the *Einstein Observatory* (MG). On the other hand, our upper limit is substantially less than the value implied by the calculations of Martin & Rouleau (1991) of the extinction and scattering cross sections of solid grains with a power-law size distribution $n(a) \sim a^{-3.5}$, 0.005 μm $< a <$ 0.25 μm, and composed of "astronomical silicate" ($R_{XV} = 0.22$ mag^{-1}) or a mixture of silicate and graphite ($R_{XV} = 0.11$ mag^{-1}). This result lends support to the idea (Mathis & Whiffen 1989) that interstellar grains may be loose, "fluffy" aggregates of smaller solid particles. The R_{XV} value for such grains is less than for solid particles of the same material because the X-ray scattering efficiency decreases more rapidly with decreasing bulk density than does the optical extinction.

We thank T. Kallman for providing us with the XSTAR code and for his assistance in applying it to our computations, and K. Arnaud for help in installing the XSPEC code on our computer system. G. C. and J. W. thank the Institute for Space and Astronautical Science and the ISAS X-ray Astronomy Group for their hospitality during extended visits. We thank the *Ginga* staff for assistance in the observations and data reduction. We are especially grateful to the referee, C. Mauche, for critical comments and numerous suggestions that stimulated extensive correction and revision of the manuscript. This research was supported in part by grant NAG 8-701 from the National Aeronautics and Space Administration.

REFERENCES

Abbott, D. C. 1980, ApJ, 242, 1183
———. 1982, ApJ, 259, 282
Alcock, C., & Hatchett, S. 1978, ApJ, 222, 456
Blondin, J. M., Kallman, T. R., Fryxell, B. A., & Taam, R. E. 1990, ApJ, 356, 591
Bradley, J. P., Humecki, H. J., & Germani, M. S. 1992, ApJ, 394, 643
Cassinelli, J. P. 1979, ARA&A, 17, 275
Cassinelli, J. P., Waldron, W. L., Sanders, W. T., Harnden, F. R., Jr., Rosner, R., & Vaiana, G. S. 1981, ApJ, 250, 677
Castor, J. I., Abbott, D. C., & Klein, R. I. 1975, ApJ, 195, 157
Catura, R. C. 1983, ApJ, 275, 645
Clark, G. W., Minato, J. R., & Mi, G. 1988, ApJ, 324, 974
Clark, G. W., Woo, J. W., Nagase, F., Makishima, K., & Sakao, T. 1990, ApJ, 353, 274
Corbet, R. H. D., Woo, J. W., & Nagase, F. 1993, A&A, 276, 52
Crampton, D., Hutchings, J. B., & Cowley, A. P. 1978, ApJ, 225, L63
Day, C. S. R., & Stevens, I. R. 1993, ApJ, 403, 322
Day, C. S. R., & Tennant, A. F. 1991, MNRAS, 251, 76
Friend, D. B., & Abbott, D. C. 1986, ApJ, 311, 701
Gorenstein, P. 1975, ApJ, 198, 95
Grindlay, J. E. 1979, ApJ, 232, L33
Haberl, F., White, N. E., & Kallman, T. R. 1989, ApJ, 343, 409
Hayakawa, S. 1970, Prog. Theor. Phys., 43, 1224
Hayashida, K., et al. 1989, PASJ, 41, 373
Kallman, T. R., & McCray, R. 1982, ApJS, 50, 263
Kitamoto, S., Miyamoto, S., & Yamamoto, T. 1989, PASJ, 41, 81
Krolik, J. H., & Kallman, T. R. 1984, ApJ, 286, 366
Krolik, J. H., & Raymond, J. C. 1985, ApJ, 298, 660
Lewis, W., Rappaport, S., Levine, A., & Nagase, F. 1992, ApJ, 389, 665
Lucy, L. B., & Solomon, P. M. 1970, ApJ, 159, 879
Lucy, L. B., & White, R. L. 1980, ApJ, 241, 300
Lucy, L. B. 1982, ApJ, 255, 286
Lucy, L. B. 1984, ApJ, 284, 351
MacGregor, K. B., Hartman, L., & Raymond, J. C. 1979, ApJ, 231, 514
Makino, F., and the Astro-C Team. 1987, Ap. Lett. Comm., 25, 223
Makishima, K., Koyama, K., Hayakawa, S., & Nagase, F. 1987, ApJ, 314, 619
Martin, P. G. 1970, MNRAS, 149, 221
Martin, P. G., & Rouleau, F. 1991, in Extreme Ultraviolet Astronomy, ed. R. F. Malina & S. Bowyer (New York: Pergamon) 341
Mathis, J. S., Rumpl, W., & Nordsieck, K. H. 1977, ApJ, 217, 425 (MRN)
Mathis, J. S., & Whiffen, G. 1989, ApJ, 341, 808
Mauche, C. W., & Gorenstein, P. 1986, ApJ, 302, 371 (MG)
McKee, C. F., & Hollenbach, D. J. 1980, ARA&A, 18, 219
Mitsuda, K., Takeshima, T., Kii, T., & Kawai, N. 1990, ApJ, 353, 480
Morrison, R., & McCammon, D. 1983, ApJ, 270, 119
Nelson, G. D., & Hearn, A. G. 1978, A&A, 65, 223
Overbeck, J. 1965, ApJ, 141, 864
Owocki, S. P., & Rybicki, G. B. 1984, ApJ, 284, 384
Poe, C. H., Owocki, S. P., & Castor, J. I. 1990, ApJ, 358, 199
Predehl, P., Baüuninger, H., Burkert, W., & Schmitt, J. H. M. M. 1991, A&A, 246, L40
Prinja, R. K., Howarth, I. D., & Henrichs, H. F. 1987, ApJ, 317, 389
Reynolds, A. P., Bell, S. A., & Hilditch, R. W. 1992, MNRAS, 256, 631
Sato, N., et al. 1986, PASJ, 38, 731
Schreier, E., Levinson, R., Gursky, H., Kellogg, E., Tananbaum, H., & Giacconi, R. 1972, ApJ, 172, L79
Spitzer, L. 1978, Physical Processes in the Interstellar Medium (New York: Wiley)
Turner, M., et al. 1989, PASJ, 41, 345
Van Blerkom, D. 1978, ApJ, 221, 186
van de Hulst, H. C. 1981, Light Scattering by Small Particles (New York: Dover)
Wood, K. S., et al. 1984, ApJS, 56, 507
Xu, Y., McCray, R., & Kelley, R. 1986, Nature, 319, 652